Research Article Vol. 28, No. 20 / 28 September 2020 / *Optics Express* 29202

Optics EXPRESS

Measuring grain size fractions of bidisperse granular materials using X-ray radiography

ERANGA DULANJALEE, FRANÇOIS GUILLARD, JAMES BAKER, ITAI EINAV, AND BENJY MARKS*

School of Civil Engineering, The University of Sydney, Sydney, NSW 2006, Australia
*benjy.marks@sydney.edu.au

Abstract: The mechanical properties of granular materials such as sand, snow and rice are inherently tied to the size of the constituent particles. When a system is composed of particles of various sizes, it is common for these particles to segregate by size when disturbed. There is therefore a need to measure the particle size distribution within granular media as it evolves over time. However, there are very few experimental techniques available which can measure the particle sizes *in situ* without disturbing the medium. Here we present a technique to determine the volume fractions of the grain sizes in bidisperse granular materials with the aid of dynamic X-ray radiography. As a result of the penetration of the X-rays into the medium, radiography minimises the effect of walls and boundaries on experimental measurements, which typically dominate optical measurements. The technique proposed here is based on using Fourier transforms of X-ray radiographs to extract local measurements evolving over time that can be related to the particle size distribution. For the case of bidisperse granular media, with two distinct particle sizes, we show that this technique can measure the relative concentration of the two species, which we determine via a heuristic calibration parameter. We validate this technique by comparing discrete element simulations of mixtures of known concentration with experimental measurements derived from X-ray radiography of glass beads. In the future, this technique could be used to measure the grain size distribution in systems of bidisperse dense granular media where the concentration of particles is not known *a priori*. Additionally, the technique can be used to analyse granular segregation as it evolves dynamically.

1. Introduction

Granular materials are widely distributed in nature and handled across various disciplines including engineering, geophysics, biology and chemical science [1,2]. The inherent heterogeneous internal structure of granular materials arises from the variability in grain size and shape, density, inelastic properties and roughness [3]. Their internal structural characteristics and physical properties determine the behavior of granular materials when they are subjected to external forces. As a result of these external forces, granular materials tend to exhibit complex patterns [4].

The grain size distribution affects the arrangement of particles and the contact network of granular systems. Hence, it is a key feature determining the packing characteristics and micro-mechanical properties of the medium [5]. The importance of measuring the grain size distribution of granular materials has been highlighted in previous studies, as grain size influences crucial properties such as hydraulic conductivity [6], shear strength [7], critical state behavior [8], pore structure [9], and segregation in dense granular flows [10]. The grain size distribution plays a key role in internal deformations [11], frontal segregation in leveed deposits [12], granular segregation down inclined planes [13] and heap formation [14]. It is also pivotal in erosion and bed stability [15], and particle interaction and energy dissipation of flowing granular media [16].

Determination of the grain size distribution of natural granular flows is challenging due to their opacity. In laboratory scale granular flow experiments, several techniques have been applied to make such measurements. For example, in flume experiments, different coloured particles have

#401021 https://doi.org/10.1364/OE.401021
Journal © 2020 Received 25 Jun 2020; accepted 7 Sep 2020; published 16 Sep 2020

been used for erodible beds and the oncoming flow to enable differentiation of materials. This technique allowed estimation of the grain size fractions inside the flowing material by examining the coloured particles at the sidewall [17]. Some studies let particles flow into a bin and sieved them to obtain grain size fractions [18], while other studies have divided the flow using a series of splitter plates to force different particles at different locations to fall into separate collector bins [19]. These approaches have limitations in spatial resolution, accuracy and laboriousness when conducting multiple trials.

To overcome these limitations, many technologies have been applied to study the internal micro-mechanics of granular materials, including Magnetic Resonance Imaging (MRI) [20,21], Positron Emission Particle Tracking (PEPT) [22,23], X-ray computed tomography (X-ray CT) [24] and X-ray radiography [25]. Some of these methods however are either intrusive on the flow or offer limited temporal and spatial resolutions, or both.

X-ray radiography is a non-destructive investigative tool developed to provide qualitative and quantitative descriptions of materials and multi-phase flows [26]. It has long been used in many disciplines, for example in medicine, geoscience, engineering and, particularly relevant for this paper, in granular mechanics. Unlike optical imaging methods, X-ray radiography minimises the effect of unrepresentative boundary layers that exist adjacent to the boundaries of experiments, capturing the behaviour through the whole depth of the sample.

Several experimental efforts and theoretical frameworks have been developed to determine the grain size distribution of particle mixtures using X-rays [27–29]. The work of [27] introduced a technique to measure the particle size distribution from a single projection image using propagation-based phase contrast X-ray imaging (PCXI). This approach was developed for opaque samples of particle volume fraction less than ten percent. The particle size distribution was estimated based on the spatial auto-correlation function (SAF). Using experiments and simulations, the SAF of a projected image was shown to be equal to the weighted sum of the SAF of each single particle size for a simple bidisperse mixture. This method was further advanced in [28] to recover the structural parameters of randomly packed spherical glass beads, based on a genetic algorithm (GA). The GA is capable of recovering the morphological parameters of the particles, and eliminating the low packing fraction constraint. In addition, the size distribution of non-spherical pores or particles was determined by [29] from single X-ray phase contrast images. A mathematical model was developed to estimate the mean pore radius in the medical context of measuring lung air volumes. This was extended to generate an expression to additionally obtain the grain size distribution. The expression was validated with simulated images and experimental data. These attempts were developed to quantify randomly packed particle systems or porous materials of non-evolving systems. For granular materials, [25] developed a methodology to measure the grain size, orientation, and internal kinematics of flowing granular media using X-ray radiography. However the method was only applicable for monodisperse materials with known size.

The purpose of this paper is to propose a method to measure the grain size fractions of evolving bidisperse materials of known particle sizes using X-ray radiography. In this case, the grain size fraction is uniquely defined by the concentration of a single species. The previous approaches were developed to quantify non-evolving systems and the analysis was associated with numerous discrete element modelling (DEM) simulations. This method is a new and convenient approach to determine the grain size fractions of evolving bidisperse granular systems.

2. Methodology

We develop here an experimental approach to determine the particle size fractions of an evolving bidisperse mixture using dynamic X-ray radiography, and validate the method using DEM simulations.

2.1. Experimental configuration

The experimental set up consists of a 3D-printed rectangular box made of polylactic acid plastic (PLA) with dimensions of 10 cm x 10 cm x 10 cm, as shown in Fig. 1(a). An insert of corrugated plastic sheet (thickness 5 mm) is placed into the container to partition the volume into two separate sub-volumes. By moving this partition, the relative volume of these two sub-volumes can be controlled, as shown in Fig. 1(b). The sub-volume closest to the X-ray source is filled with the larger sized glass beads and the other is filled with the smaller sized glass beads. This split box removes the problem of granular segregation discussed above and allows for accurate control of the effective relative particle concentration.

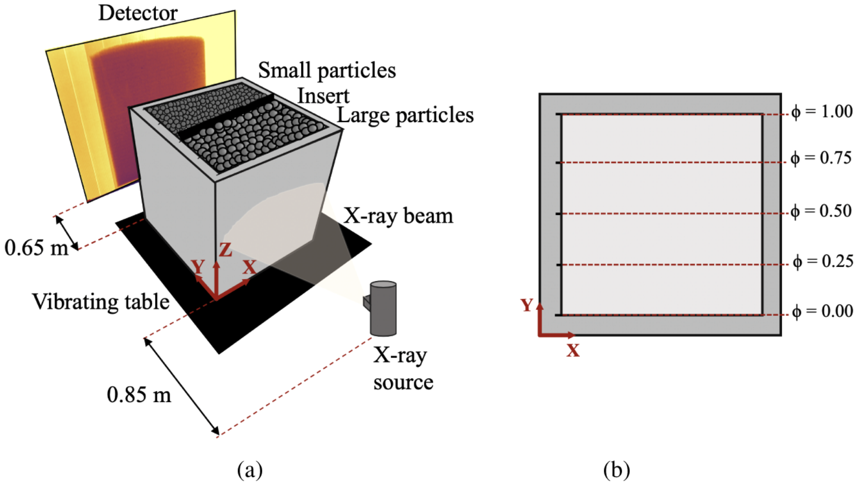

(a) (b)

Fig. 1. (a) Schematic representation of the experimental setup with particles of two different sizes in adjacent sub-volumes. (b) Top view of the empty box marked with the positions of the insert (Red dotted lines indicate the large particle concentrations at each insert position).

The system is placed on a vibration stage and vibrated at a low amplitude to slowly change the configuration state of the grains. The purpose of vibrating the system is to generate an evolving system. Hence, the calibration methodology can be directly applied to similar evolving granular systems. The total experimental programme involves combinations of three sizes of glass beads, 0.5 mm, 1 mm and 3 mm diameter. Accordingly, three sets of experiments were performed with different size ratios $R = d_l/d_s$ of large (d_l) to small (d_s) particle diameters.

The motion of the glass beads within the box was captured by X-ray radiography. A Varian NDI-225-21 X-ray tube was used to emit radiation at a maximum energy of 160 keV and intensity of 5 mA. The radiation passed through the grains in the box and the transmitted radiation was recorded on a PaxScan 2520DX detector panel at a resolution of 768 px × 960 px and a recording speed of 30 frames per second for the 1 mm and 3 mm glass bead combinations. The experiments with 0.5 mm glass beads data were recorded on a Dexela 2923 NDT detector at a resolution of 3072 px × 3888 px and recording speed of 25 frames per second.

2.2. X-ray attenuation

The measured intensity of X-rays (I) at a location $\mathbf{x}$ on the detector panel can be approximated by [30],

$$I(\mathbf{x}) = I_0 \exp\left(-\int \mu(l)\, dl\right), \tag{1}$$

where I_0 is the intensity of the source and $\mu(l)$ is the attenuation coefficient for the X-ray radiation, at a location l along the line of sight between the X-ray source and the pixel of interest. As the attenuation coefficient is proportional to the density of the material [31], for materials with homogeneous chemical composition, the radiographs provide a local measurement of density averaged along the path of the ray.

2.3. Discrete element modelling

Simulations were undertaken to validate the results obtained from the experiments. The DEM tool MercuryDPM [32] was used to generate and model the bidisperse granular assembly. Particles were generated at a known volume fraction and bidisperse concentration, and randomly positioned in a rectangular volume of 20 mm x 20 mm x 100 mm with Lees-Edwards boundary conditions in the first two dimensions and periodic boundary conditions in the remaining (longest) dimension. This set of boundary conditions were used to control both the total solids fraction and relative grain size fractions with no segregation whilst simultaneously agitating the grains. The system was sheared at a rate of 0.5 s^{-1}. The rectangular volume was filled with the large and small particles until the system achieved a target volume fraction and concentration of the two particle sizes. Particle interactions in the normal direction were linear viscoelastic. In the tangential and rolling directions a frictional linear viscoleastic model was used. The density, coefficient of restitution, sliding friction coefficient, rolling resistance coefficient and collision time were set as 2500 kg/m^3, 0.8, 0.5, 0.001 and 0.001 s respectively, with the stiffness and damping coefficients calculated from these values. These values are representative for typical glass beads [33]. For each particle size ratio (R), simulations were performed for large particle concentration values (ϕ) of 0, 0.25, 0.5, 0.75 and 1 and at solid fractions of 0.5, 0.6 and 0.7.

The DEM simulation output contains the spatial coordinates of all particles at time steps of 0.01 s. Based on these positions, artificial radiographs were generated using Eq. (1), with a resolution of 8000 pixels/m to maintain a similar resolution to the experiments. The initial X-ray intensity (I_0) and attenuation coefficient (μ) were set as 1 m^{-1} and 0.2 respectively to produce images with suitable contrast and to reflect the experimental measurements. These artificial radiographs are produced assuming a parallel X-ray source, monochromatic beam and zero noise level. In addition to the bidisperse mixtures, artificial radiographs of the segregated experimental configuration (with bulk material of different size physically separated) were produced by overlaying various thicknesses of the equivalent monodisperse flows produced as described above.

2.4. Bidisperse concentration measurement

The bidisperse particle concentration measurement follows the methodology developed by [25] for measuring the characteristic size of monodisperse particles. This technique uses X-ray radiography to determine bulk material properties from the inherent density fluctuations of the material. The bidisperse measurement methodology is based around the two-dimensional Fourier transformation, and is summarized in Fig. 2.

Firstly the initial radiograph is subdivided into square patches of width $w = 64$ pixels (Fig. 2(a)). Each patch is normalised such that it has zero average intensity and a standard deviation of unity. A radial hamming window, $\mathcal{W}(r)$, is then applied,

$$\mathcal{W}(r) = \frac{1}{2}\cos\left(\frac{2\pi r}{w}\right), \tag{2}$$

where r is the distance from the centre of the patch. A two-dimensional Fourier transform is performed on each patch to obtain the power spectrum S, as

$$S(\mathbf{k}) = \left|\iint I(\mathbf{x}) \times \mathcal{W}(r(\mathbf{x}))\exp(2i\pi\mathbf{k}\cdot\mathbf{x})\,d\mathbf{x}\right|^2, \tag{3}$$

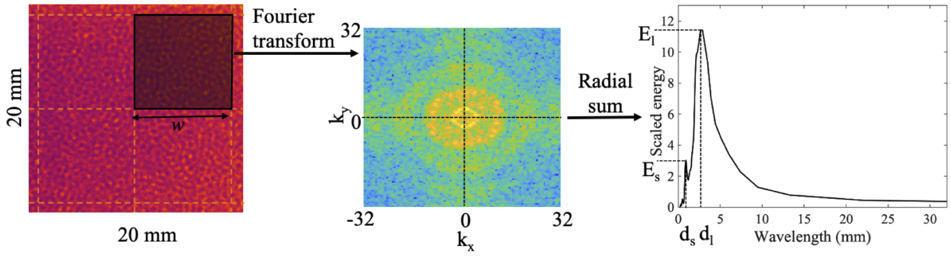

(a) Radiograph (b) Energy spectrum (c) Radial energy distribution

Fig. 2. Determination method of bidisperse concentration (simulation R=3 and ϕ=0.5) (a) Initial radiograph indicating the patches of 64×64 pixels (b) Energy spectrum of the patch (after multiplication by a circular hamming window and processed by two-dimensional Fourier transformation) (c) The radial energy distribution as a function of the radius.

where $I(\mathbf{x})$ is the normalised X-ray intensity of the pixel at location $\mathbf{x}$ in the patch and $\mathbf{k}$ is the wavevector. In Fig. 2(b), the power spectrum of the patch shows two rings which correspond to the two grain sizes in the bidisperse mixture. Fig. 2(c) contains the orthoradially summed energy spectrum as a function of wavelength, which is found by taking annular sums over the data in Fig. 2(b). Each spectral ring indicated in the energy spectrum corresponds to a peak at a characteristic wavelength (indicated at d_l and d_s), and is related to a particle size in the bidisperse mixture. The peak heights corresponding to each particle size (E_l and E_s are the peak heights within ±0.3 mm of the large and small particle sizes) indicate orthoradially summed energy values of the power spectrum as shown in Fig. 2(c). Representative energy values were obtained by averaging the energy distribution function of each patches, since the experiments and simulations are steady-state and homogeneous in the plane of the radiographs.

We introduce the *peak fraction*, F, as a measurable heuristic quantity derived from the energy spectrum peaks, namely

$$F = \frac{E_l}{E_s + E_l}. \tag{4}$$

The remainder of this paper investigates the relationship between F and the corresponding concentration of the bidisperse mixture.

3. Results and discussion

Four examples of the measured energy spectra are shown in Fig. 3. These spectra have been averaged over 4000 patches (produced at different spatial locations and times), and one standard deviation around this mean value is shown in grey. In each image, two distinct peaks are visible, corresponding to the two particle sizes in the mixture, and are marked with dashed lines. We note that particle sizes can only be identified reliably if the frequency corresponding to their diameter is less than the Nyquist frequency. The peaks evolve as expected as the volume fraction of large particle increases, with an increase of the large particle energy peak and a decrease of the small particle one. It is clear however that the size of the particles themselves plays a significant role, the peak of energy for the large particles getting more intense as the large particle size increases.

To investigate how many patches are required to saturate a given measurement, Fig. 4 shows the variation of the normalised standard deviation (standard deviation divided by the mean value and the square root of the number of patches) at small and large grain sizes for size ratios $R = 2$ and 6 as a function of the number of patches. In general, these standard deviations saturate at approximately 4000 patches, and this value is used to produce the remainder of the data in this work.

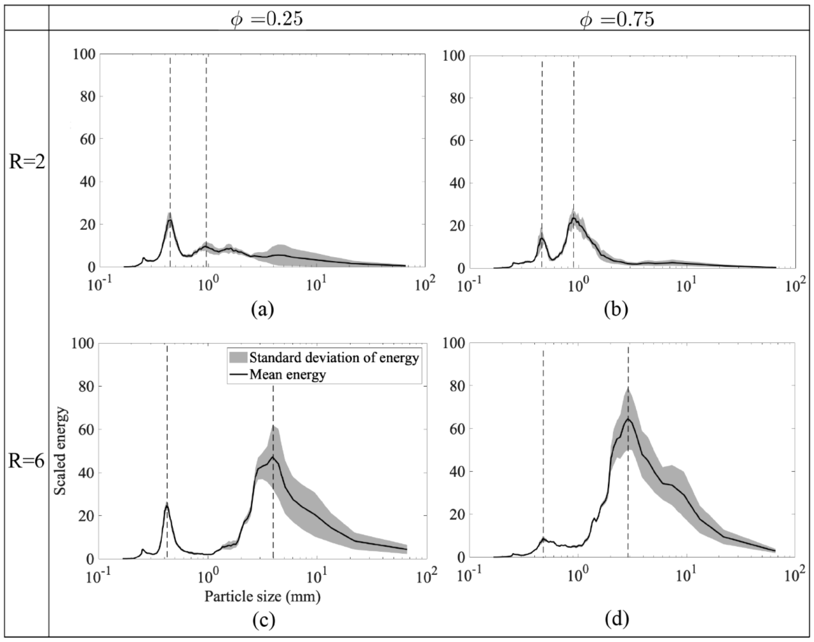

Fig. 3. Examples of the measured ortho-radially summed FFTs extracted from DEM simulations. Black line represents the mean energy averaged over 4000 patches, grey area indicates one standard deviation of the energy. Dotted black line indicates the position of the peak given the grain size (a) ϕ =0.25 and R =2, (b) ϕ =0.75 and R =2, (c) ϕ =0.25 and R =6, (d) ϕ =0.75 and R =6.

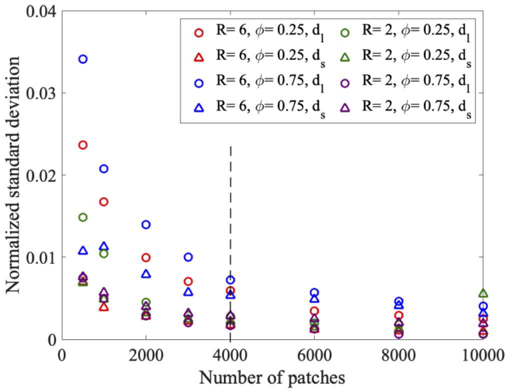

Fig. 4. Variation of normalised standard deviation as a function of the number of patches averaged from DEM simulation data.

Figure 5(a) illustrates the calibration curves from DEM simulations using different solid fractions. The curves overlap significantly for solids fractions of 0.5 and 0.6, whereas the curve for solid fraction of 0.7 has a slight deviation. The error bars on Fig. 5(a) are calculated based on one standard deviation of the energy. Comparison of the error bars for different solid fractions indicate that the measurement technique is largely insensitive to the solids fraction in this range, which is larger than that typical for dense flows. According to the interpretation of [34], the radial distribution function is persistent for different polydispersity. The peak fraction variation of different patch sizes for simulations and experiments are shown in Fig. 5(b). The peak fraction

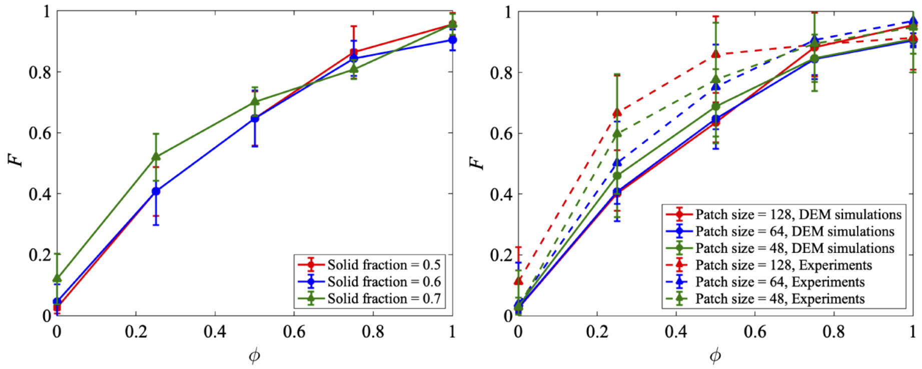

(a) (b)

Fig. 5. Calibration curves comparison (examples from R=3) (a) Different solid fractions (b) Experiments and simulations of different patch sizes.

variation for different patch sizes for simulations indicates that for large patch sizes similar results can be obtained. In the smallest patch size the associated error is higher than the other patch sizes. The experimental peak fraction variation therefore depends on the patch size.

Figure 6 illustrates the variation in peak fraction as a function of the concentration of large particles for different particle size combinations. Experimental data (where particles species are separated by a partition) is compared against DEM data of mixed grains, and fully segregated grains in the same configuration as the experiment. In all cases, the peak fraction increases with increasing large particle volume fraction ϕ, and there is relatively good agreement between the

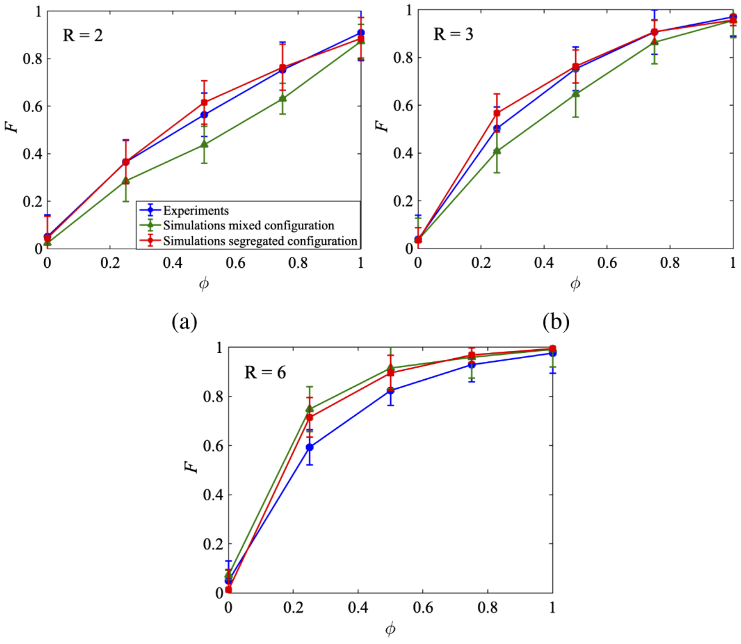

(a) (b)

(c)

Fig. 6. Simulations (mixed and segregated particle configuration) and experimental calibration curves of different grain size combinations (a) R=2, (b) R=3, (c) R=6.

DEM simulations in the segregated configuration and the experimental data. However, it is clear that this measurement technique gives different results depending on whether particles are mixed together or segregated. We interpret this behaviour as the ability of the measurement technique to quantify the radial distribution function of the medium [34]. When ϕ=0 and ϕ=1, the F values deviate from the expected F=0 and F=1 for two reasons. Firstly, we observe additional Fourier peaks beyond the first mode (which is at the particle size), and secondly, as a result of noise both in the radiographs (which is only present in experimental radiographs) and due to the relatively small patch sizes relative to the particle size. The highest standard deviations are observed for the largest particles, presumably as there are fewer of these particles per patch due to their size.

The difference between the experiments and simulations in the mixed particle configuration in Figure 6 can be explained from the difference in particle mixing. In DEM simulations, particles are added and mixed randomly, while in the experiments the particles are physically separated. In addition, the cone shaped geometry of the X-ray beam in the experiments delivers a magnified grain size of the particle to the detector [35]. The artificial radiographs generated from the simulations assume that the X-ray beam is parallel. In addition, a polychromatic X-ray source is used in the experiments, which is different to the monochromatic one used to generate the artificial radiographs, and this may also contribute to the discrepancy in the results due to beam hardening effects. Finally, scattering occurs when X-rays pass through the material, which can deteriorate the image quality with low image contrast and poor uniformity [36]. This scattering is not taken into account when generating the X-ray radiographs from the simulations.

4. Conclusion

In this paper we have outlined a technique to measure the grain size fractions of evolving bidisperse granular materials with the aid of dynamic X-ray radiography. The technique proposed is based on Fourier transforms of X-ray radiographs to extract spatiotemporal measurements that can be correlated with the particle sizes. This method provides a measurement of the relative concentration of two distinct species via a heuristic calibration parameter, which we term the peak fraction. Validation of the technique using discrete element method simulations with spheres of known concentration against experimental measurements demonstrates good accuracy. The results are independent of the solid fraction of the system for the range of solids fractions typically observed in dense granular flows. This technique can be used to calibrate grain size volume fraction measurements, providing crucial information to investigate the behavior of bidisperse granular systems. In the future, the technique could be developed to measure the grain size volume fractions in system of dense granular media where the concentration of the particles is not known *a priori*, and beyond bidisperse mixtures. Additionally, the technique can be further used to analyse granular segregation, mixing and particle breakage.

Funding

Australian Research Council GA68758.

Disclosures

The authors declare no conflicts of interest.

References

1. D. Buscombe and D. M. Rubin, "Advances in the simulation and automated measurement of well-sorted granular material: 1. simulation," J. Geophys. Res. Earth Surf. **117**(F2), 1974 (2012).
2. A. D. Rosato, D. L. Blackmore, N. Zhang, and Y. Lan, "A perspective on vibration-induced size segregation of granular materials," Chem. Eng. Sci. **57**(2), 265–275 (2002).
3. D. R. Tunuguntla, T. Weinhart, and A. R. Thornton, "Comparing and contrasting size-based particle segregation models: Applying coarse-graining to perfectly bidisperse systems," Comput. particle mechanics **4**(4), 387–405 (2017).

4. G. Metcalfe and M. Shattuck, "Pattern formation during mixing and segregation of flowing granular materials," Phys. A: Stat. Mech. its Appl. **233**(3-4), 709–717 (1996).
5. N. Kruyt, "Micromechanical study of elastic moduli of three-dimensional granular assemblies," Int. J. Solids Struct. 51 **51**(13), 2336–2344 (2014).
6. J. M. Sperry and J. J. Peirce, "A model for estimating the hydraulic conductivity of granular material based on grain shape, grain size, and porosity," Groundwater **33**, 892–898 (1995).
7. E. Azéma, S. Linero, N. Estrada, and A. Lizcano, "Does modifying the particle size distribution of a granular material (i.e., material scalping) alters its shear strength?," in *Powders and Grains 2017*, vol. v1 (2017).
8. M. D. Jiang, Z. X. Yang, D. Barreto, and Y. H. Xie, "The influence of particle-size distribution on critical state behavior of spherical and non-spherical particle assemblies," Granul. Matter **20**(4), 80 (2018).
9. Y. Liu and D.-S. Jeng, "Pore structure of grain-size fractal granular materials," Materials **12**(12), 1996 (2019).
10. J. M. N. T. Gray, "Particle segregation in dense granular flows," Annu. Rev. Fluid Mech. **50**(1), 407–433 (2018).
11. A. Billi, "Grain size distribution and thickness of breccia and gouge zones from thin (<1 m) strike-slip fault cores in limestone," J. Struct. Geol. **27**(10), 1823–1837 (2005).
12. C. G. Johnson, B. P. Kokelaar, R. M. Iverson, M. Logan, R. G. LaHusen, and J. M. N. T. Gray, "Grain-size segregation and levee formation in geophysical mass flows," J. Geophys. Res. Earth Surf. **117**(D20), 16760 (2012).
13. B. Marks, P. Rognon, and I. Einav, "Grainsize dynamics of polydisperse granular segregation down inclined planes," J. Fluid Mech. **690**, 499–511 (2012).
14. Y. Fan, P. B. Umbanhowar, J. M. Ottino, and R. M. Lueptow, "Kinematics of monodisperse and bidisperse granular flows in quasi-two-dimensional bounded heaps," Proc. Royal Soc. A: Math. Phys. Eng. Sci. **469**(2157), 20130235 (2013).
15. J. C. Mullarney Staudt, "The role of grain-size ratio in the mobility of mixed granular beds," Geomorphology **278**, 314–328 (2017).
16. B. Cagnoli and A. Piersanti, "Grain size and flow volume effects on granular flow mobility in numerical simulations: 3-D discrete element modeling of flows of angular rock fragments," J. Geophys. Res. Solid Earth **120**, 2350–2366 (2015).
17. G. B. Crosta, F. V. De Blasio, M. De Caro, G. Volpi, S. Imposimato, and D. Roddeman, "Modes of propagation and deposition of granular flows onto an erodible substrate: experimental, analytical, and numerical study," Landslides **14**(1), 47–68 (2017).
18. D. Moberly, "Laboratory experiments investigating entrainment by debris flows," Master's thesis, University of Minnesota (2015).
19. S. B. Savage and C. K. K. Lun, "Particle size segregation in inclined chute flow of dry cohesionless granular solids," J. Fluid Mech. **189**, 311–335 (1988).
20. R. Stannarius, "Magnetic resonance imaging of granular materials," Rev. Sci. Instruments **88**(5), 051806 (2017).
21. M. Nakagawa, S. A. Altobelli, A. Caprihan, E. Fukushima, and E.-K. Jeong, "Non-invasive measurements of granular flows by magnetic resonance imaging," Exp. Fluids **16**(1), 54–60 (1993).
22. A. Buffler, K. Cole, T. Leadbeater, and M. van Heerden, "Positron emission particle tracking: A powerful technique for flow studies," Int. J. Mod. Physics: Conf. Ser. **48**, 1860113 (2018).
23. D. Parker, A. Dijkstra, T. Martin, and J. Seville, "Positron emission particle tracking studies of spherical particle motion in rotating drums," Chem. Eng. Sci. **52**(13), 2011–2022 (1997).
24. Z. Karatza, E. Andò, S.-A. Papanicolopulos, G. Viggiani, and J. Y. Ooi, "Effect of particle morphology and contacts on particle breakage in a granular assembly studied using X-ray tomography," Granul. Matter **21**(3), 44 (2019).
25. F. Guillard, B. Marks, and I. Einav, "Dynamic X-ray radiography reveals particle size and shape orientation fields during granular flow," Sci. Rep. **7**(1), 8155 (2017).
26. T. J. Heindel, "A review of X-ray flow visualization with applications to multiphase flows," J. Fluids Eng. **133**(7), 074001 (2011).
27. R. P. Carnibella, M. J. Kitchen, and A. Fouras, "Determining particle size distributions from a single projection image," Opt. Express **20**(14), 15962–15968 (2012).
28. R. P. Carnibella, M. J. Kitchen, and A. Fouras, "Decoding the structure of granular and porous materials from speckled phase contrast X-ray images," Opt. Express **21**(16), 19153–19162 (2013).
29. A. F. T. Leong, E. Asare, R. Rex, X. H. Xiao, K. T. Ramesh, and T. C. Hufnagel, "Determination of size distributions of non-spherical pores or particles from single X-ray phase contrast images," Opt. Express **27**(12), 17322–17347 (2019).
30. E. Krinitzsky, *Radiography in the earth sciences and soil mechanics*, Monographs in geoscience (Plenum Press, 1970).
31. J. Hubbell, "Photon mass attenuation and energy-absorption coefficients," The Int. J. Appl. Radiat. Isot. **33**(11), 1269–1290 (1982).
32. T. Weinhart, D. Tunuguntla, M. Lantman, I. Denissen, C. Windows Yule, H. Polman, J. Tsang, B. Jin, L. Orefice, K. Vaart, S. Roy, H. Shi, A. Pagano, W. DenBreeijen, B. Scheper, A. Jarray, S. Luding, and A. Thornton, "MercuryDPM: Fast, flexible particle simulations in complex geometries part II: Applications," *Computational particle mechanics* pp. 123–134 (2017).

33. R. Fuchs, T. Weinhart, J. Meyer, H. Zhuang, T. Staedler, X. Jiang, and S. Luding, "Rolling, sliding and torsion of micron-sized silica particles: experimental, numerical and theoretical analysis," Granul. Matter **16**(3), 281–297 (2014).
34. S. Zhao, J. Zhao, and N. Guo, "Universality of internal structure characteristics in granular media under shear," Phys. Rev. E **101**(1), 012906 (2020).
35. L. Babout, B. Karpiski, and M. Szkodo, "Selection of material for X-ray tomography analysis and dem simulations: comparison between granular materials of biological and non-biological origins," Granul. Matter **20**(3), 38 (2018).
36. T. Tien-Hsiu and K. Ikuo, "A simulation study on the influence of scattered X-rays in energy-resolved computed tomography," J. Nucl. Sci. Technol. **54**(2), 205–212 (2017).